LASER INTERFEROMETER GRAVITATIONAL WAVE OBSERVATORY
- LIGO -
CALIFORNIA INSTITUTE OF TECHNOLOGY
MASSACHUSETTS INSTITUTE OF TECHNOLOGY

Technical Note	LIGO-T1500485–v1	2015/10/17

A prototype for a tilt-free seismometer

Alessandra Marrocchesi | Mentors: Kate Dooley, Koji Arai, Rana Adhikari

California Institute of Technology
LIGO Project, MS 18-34
Pasadena, CA 91125
Phone (626) 395-2129
Fax (626) 304-9834
E-mail: info@ligo.caltech.edu

Massachusetts Institute of Technology
LIGO Project, Room NW22-295
Cambridge, MA 02139
Phone (617) 253-4824
Fax (617) 253-7014
E-mail: info@ligo.mit.edu

LIGO Hanford Observatory
Route 10, Mile Marker 2
Richland, WA 99352
Phone (509) 372-8106
Fax (509) 372-8137
E-mail: info@ligo.caltech.edu

LIGO Livingston Observatory
19100 LIGO Lane
Livingston, LA 70754
Phone (225) 686-3100
Fax (225) 686-7189
E-mail: info@ligo.caltech.edu

http://www.ligo.caltech.edu/

Abstract

Seismic noise is the most relevant noise source for LIGO at low frequencies, and it represents a main limit in the possibility of gravitational wave detection. In order to reduce this noise, different active and passive isolation systems have been developed. However present devices are affected by some limitations that should be overcome. One of these is the fact that seismometers used in active isolation can't distinguish ground motion from ground tilt at low frequencies. In order to solve this problem the design for a tilt-free seismometer was developed in the past years and a prototype of this seismometer is being built. In this paper the seismometer performance is described and my work on the prototype seismometer is presented.

Contents

1   Introduction

In this section I'm going to describe the motivations to build a tilt-free seismometer and how this seismometer can be built.

1.1   Seismic noise and isolation

LIGO is a gravitational wave observatory; it is essentially a Michelson interferometer with two arms of 4 km length. As a laser interferometer, LIGO's sensitivity is limited by three main noise sources:

- Seismic noise: noise related to vibrations of the laboratory.

- Thermal noise: noise generated by dissipation in the mirrors.

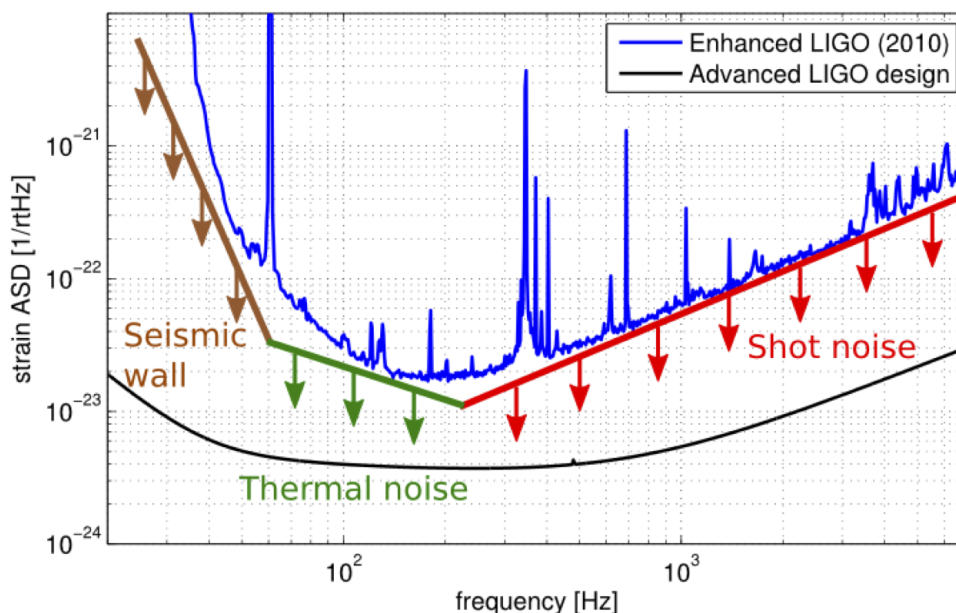- Shot noise: noise due to fluctuation of photon number in the laser beams.

Figure 1.1: LIGO noise sources

There are many other contributions to the sensitivity but here we're mostly interested in seismic noise.

1.1.1 Seismic noise

As shown in figure 1.1, seismic noise is a low frequency limit for the interferometer. Seismic noise comes from geological activity of the Earth's crust, atmospheric phenomena and human activity. Above ∼1 Hz the vibration spectra for quiet sites is given by (f is the vibration frequency):

$$x_G = 10^{-8} \left(\frac{1\ Hz}{f}\right)^2 \frac{m}{\sqrt{Hz}} \tag{1.1}$$

This affects the mirrors of the interferometer making them vibrate as the ground moves. As the interferometer needs to be capable to detect waves with an amplitude of $h \sim 10^{-21}/\sqrt{\text{Hz}}$ those vibrations are not acceptable. Thus, considering that the arms of the interferometer are 4 km long, vibrations must be suppressed by at least eight orders of magnitude at 10 Hz and six orders of magnitude at 100 Hz .

1.1.2 Passive and active isolation at LIGO

At both LIGO sites many optics need to be isolated from ground motion. This is achieved by using systems which provide active and passive isolation.

- Passive isolation consists of the use of structures with intrinsic mechanical properties that make the instruments less sensitive to ground vibrations. It is realized through the use of multiple stages platforms (different stages separated by spring assembly) for the optics and by suspending the optics themselves.

- Active isolation consists of the use of inertial sensors (e.g. seismometers) to measure ground motion (in a feedforward scheme) and platform's motion (in a feedback scheme) and then generate a counter-motion to keep the interferometer components still.

1.2 The tilt coupling problem

The use of seismometers in active isolation is limited at low frequencies by tilt of the ground, which occurs mostly in windy times.

1.2.1 The problem

Basically a seismometer is made of a case connected to the ground, containing a mass mounted on a spring-damper, which moves with respect to the case as the ground moves. The measurement of the relative motion (δ) of the mass to the case gives us the spectrum of ground motion. A simple seismometer is shown in figure 1.2:

If k is the spring constant, γ the damping constant and x the ground displacement, the equation of motion for the mass m is given by:

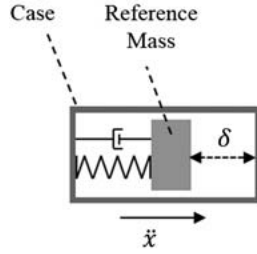$$m\ddot{\delta} + \gamma\dot{\delta} + k\delta = m\ddot{x} \tag{1.2}$$

Figure 1.2: A simple seismometer. [4]

Thus the transfer function of the seismometer in the Fourier domain (where the frequency is called ω) results in:

$$\frac{\tilde{\delta}}{\tilde{x}} = \frac{-m\omega^2}{k + i\gamma\omega - m\omega^2} \tag{1.3}$$

If we now introduce a ground tilt of a small angle θ the equation of motion for m becomes:

$$m\ddot{\delta} + \gamma\dot{\delta} + k\delta = m\ddot{x} + mg\theta \tag{1.4}$$

and we obtain:

$$\tilde{\delta} = \frac{-m\omega^2}{k + i\omega\gamma - m\omega^2} \left(\tilde{x} - \frac{g}{\omega^2}\tilde{\theta} \right) \tag{1.5}$$

It follows that ground tilt cannot be distinguished from ground displacement, and if we calculate the ratio between the tilt and translation contributions to the read-out of the sensor we find:

$$\frac{\frac{\partial \tilde{\delta}}{\partial \tilde{\theta}}}{\frac{\partial \tilde{\delta}}{\partial \tilde{x}}} = -\frac{g}{\omega^2} \tag{1.6}$$

Thus at low frequencies (typically below 100 mHz) the tilt contribution dominates over the translation contribution and the seismometer signal is too contaminated by ground tilt to be used.

1.2.2 Possible solutions

An approach to solve this problem could be to measure tilt independently and then subtract it from the seismometer measurements. However, this approach is limited by the tilt sensor noise and by errors coming from a subtraction of two large numbers.
Alternatively, we can think of building a seismometer that is made in the first place to mechanically filter out the effect of ground tilt. This has the advantage that ground displacement could be determined by only one measurement, not two.

A way to filter out tilt is to use suspended platforms. This approach is based on the principle that a mass suspended with an infinitely soft wire is unaffected by a tilt of the suspension point. Relying on this, tilt transmitted to the sensor can be reduced by placing it on a suspended structure (fig. 1.3), as explained by Matichard et al [7].
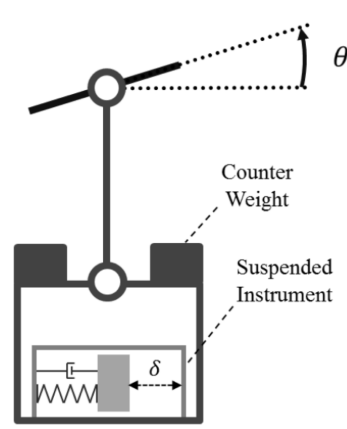

Figure 1.3: Placing a seismometer on a suspended structure reduces tilt transmission.

1.3   A new instrument to filter tilt

1.3.1   The tilt-free seismometer

Besides using a suspended platform to solve the tilt problem, a highly sensitive seismometer can be employed in order to have a very accurate measurement of ground horizontal motion. A seismometer with that high sensitivity has been designed as an inverted pendulum and a Michelson interferometer readout. Such a seismometer can be implemented in a suspended structure as in the CAD model in figure 1.4. The suspended platform, called "rhomboid" (in blue), is suspended from above using two thin steel wires (yellow) attached to an aluminum frame (red). Placed at the center of mass of the rhomboid is the inverted pendulum (green). The Michelson interferometer is built on top of the rhomboid and inverted pendulum and it measures the relative distance between these two. From this measurement we can extract the spectrum of ground motion.

1.3.2   Sensitivity limits

Both rhomboid and seismometer translation sensitivity are limited by different factors. The sensitivity limits basically come from the frequency response of an harmonic oscillator to the motion of the suspension point. Consider the seismometer analyzed in section 1.2.1. introducing the coordinate x' for the position of the mass (instead of the relative coordinate δ). If we calculate the transfer function from ground motion to mass displacement we find:

$$\frac{\tilde{x}'}{\tilde{x}} = \frac{\omega_0^2 + i\frac{\gamma}{m}\omega}{\omega_0^2 + i\frac{\gamma}{m}\omega - \omega^2} \tag{1.7}$$

where ω_0 is the harmonic oscillator resonant frequency. The shape of this transfer function is given in figure 1.5 and the shape for a pendulum frequency response to ground translation is the same.

Consider now our rhomboid. It was shown by Matichard et al. ([7]) that a structure like the rhomboid is sensitive to ground translation in the frequency region between its tilt and its pendulum resonant frequencies (see fig. 1.6). As a matter of fact, below the tilt resonant frequency, as the ground tilts, the rhomboid also tilts and it is not possible to measure ground horizontal motion: the seismometer just acts as a tilt sensor. Above the tilt resonant frequency tilt-coupling is attenuated, while below the pendulum resonant frequency the rhomboid motion follows ground translation. Thus in the region between these two fre-
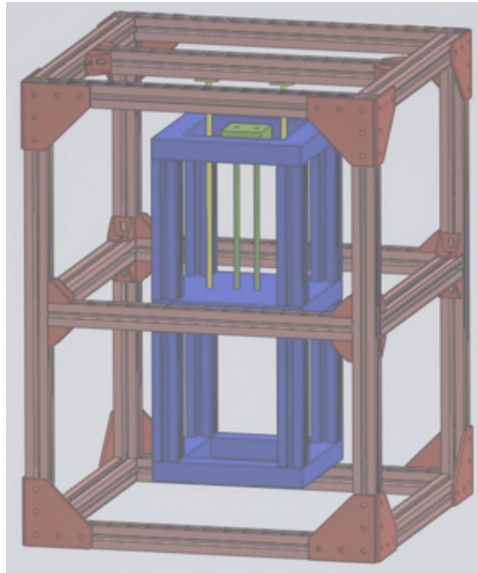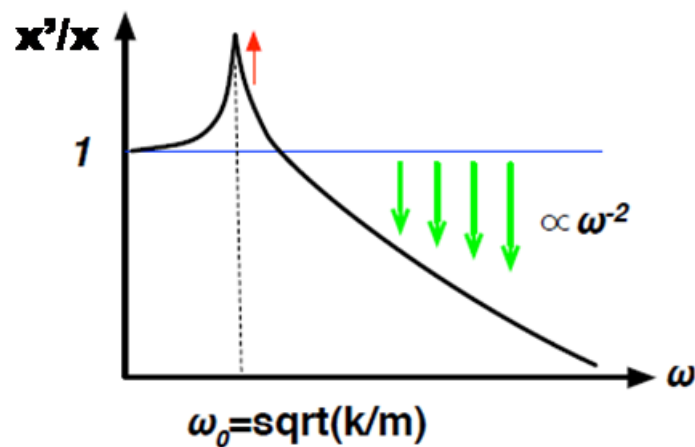
Figure 1.4: Tilt-free seismometer CAD. [5]

Figure 1.5: Frequency response of an harmonic oscillator to ground motion. [3]
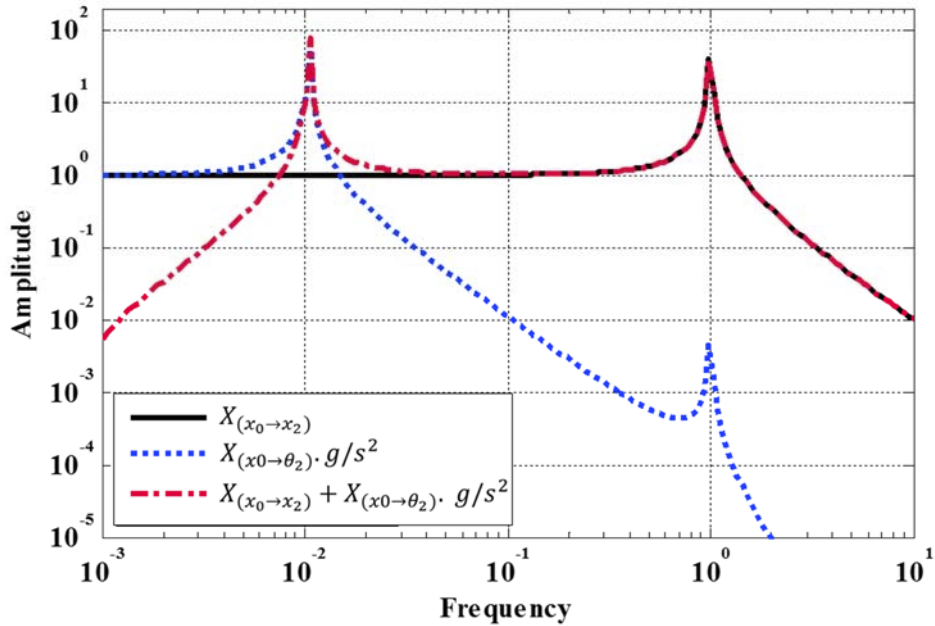
Figure 1.6: The curve of interest here is the red curve, which shows the transfer function of a suspended platform (i.e. the rhomboid) from suspension point to inertial sensor's output. [7]

quencies the seismometer is a good seismometer. Above the pendulum resonant frequency, because of the pendulum response to suspension point translation, the rhomboid can't follow ground motion and the seismometer has nothing to measure.
Thus, the rhomboid tilt and pendulum resonant frequencies put respectively a lower and upper limit to the frequency range in which we can have an accurate measurement of ground horizontal motion.

For what concerns our seismometer, from equation 1.3 we find that the seismometer translation sensitivity is low below the harmonic oscillator's resonant frequency. Thus a calibration needs to be done to make the seismometer frequency response flat, but this inevitably decreases SNR below the natural frequency.

From the above it follows that in order to increase the performarce of our tilt-free seismometer we want to reach very low (∼40 mHz) rhomboid tilt and inverted pendulum resonant frequencies.

1.3.3   Installation in LIGO

The tilt-free seismometer presented has its future location in LIGO suspended next to the test masses. It will directly measure and control the ISI stage 2 table motion.

2 Summer project

In this section I'm going to explain my work on a prototype for the tilt-free seismometer presented in the previous section. This work essentially focused on three aspects: determination of the rhomboid resonant frequencies, determination of the parameters needed for the inverted pendulum (IP) to reach a resonant frequency of ∼40 mHz, and temperature stabilization of the seismometer.

2.1 Rhomboid resonant frequencies

To characterize the rhomboid of the prototype structure it is necessary to measure its tilt, pendulum and yaw resonant frequencies. There will be two tilt and two pendulum resonant frequencies, as the rhomboid can oscillate along its long or its short side. Particularly, as explained in section 1, the seismometer sensitivity to ground motion depends on the rhomboid tilt and pendulum resonant frequencies, thus the determination of both is essential to act on the structure to increase the seismometer sensitivity region. In this paragraph the procedure used to measure the rhomboid resonant frequencies and the results for this measurement are shown.

The setup used is shown in pictures 2.1. Two mirrors are placed on the opposite short sides of the rhomboid and, correspondingly, on one side of the frame we have a fiber coupled laser, a mirror and a quadrant photodiode (QPD), while on the other we have an instrument with a LED and two photosensors. An aluminum sheet is placed on one of the two long sides of the rhomboid and correspondingly another LED and photosensors are placed on the frame. The QPD senses the rhomboid motion in the following way: the beam coming from the laser is reflected from the first mirror (on the frame) so that it can hit the center of the other mirror (on the rhomboid), be reflected again, and finally hit the QPD. As the rhomboid oscillates, the laser beam spot on the QPD moves too and the resonant frequency can be measured from the QPD output voltage.
For what concerns the photosensors we have that they receive the LED light reflected from the mirror (or the aluminum sheet) placed on the rhomboid. As the rhomboid oscillates the amount of light received by the photosensors changes too and the photosensors output voltage gives us the oscillation resonant frequency.
Resonant frequencies are measured with an oscilloscope and confirmed with a spectrum analyzer.

Before measuring the rhomboid resonant frequencies a QPD calibration has to be done in order to determine the relation between the QPD output voltage and the displacement input. In the following paragraph the procedure and results for this calibration are shown.

2.1.1 QPD calibration

The QPD used in the resonant frequencies measurement has three voltage outputs: an X output proportional to the difference between the power on the right and left sides of the QPD; an Y output proportional to difference between the power on the top and bottom sides

<table>
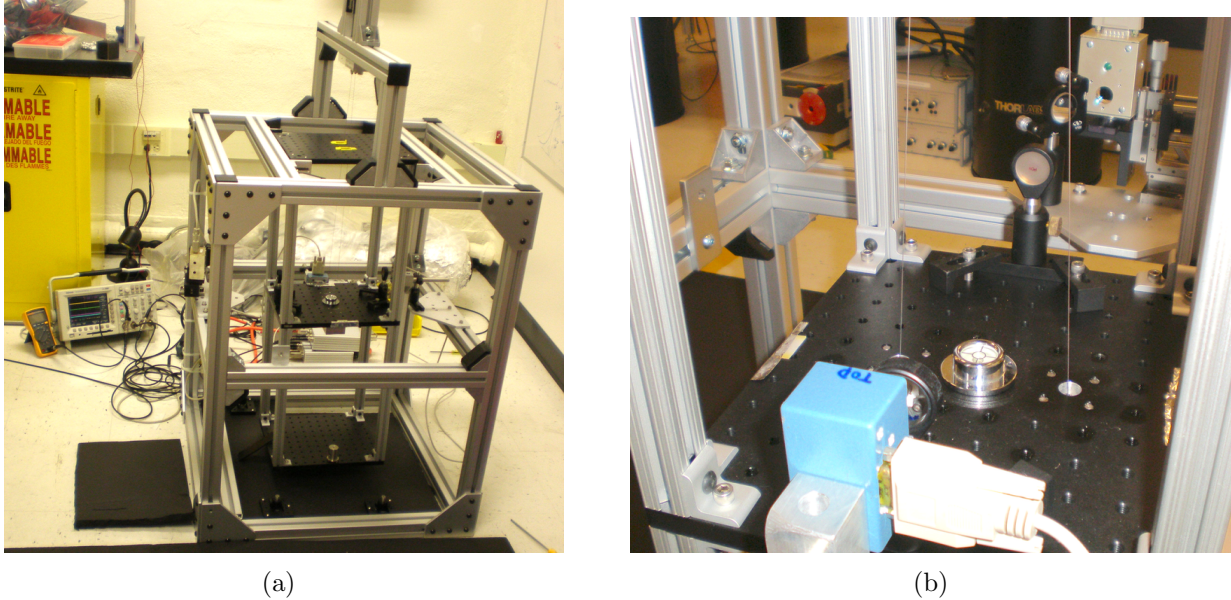<tr><td>(a)</td><td>(b)</td></tr>
</table>

Figure 2.1: Setup for rhomboid resonant frequencies measurements

of the QPD; an S output proportional to the total power on the QPD.

The procedure used for the calibration consisted of centering the laser beam on the QPD, then moving the QPD from left to right in a 3 mm range along the horizontal axis (using a sliding stage and a micrometer), and, in this range, take 30 measurements of the QPD X output using a digital multimeter. The procedure was then repeated moving the QPD along the vertical axis and taking 30 measurements of the QPD Y output.

Since the beam is gaussian, the expected calibration curve has the shape of an error function.

- X axis calibration

  Figure 2.2(a) shows the X axis QPD calibration curve and a fit is made in the linear region. Error bars were estimated from the fluctuations of the output voltage .

  The fit in the linear region with the function:

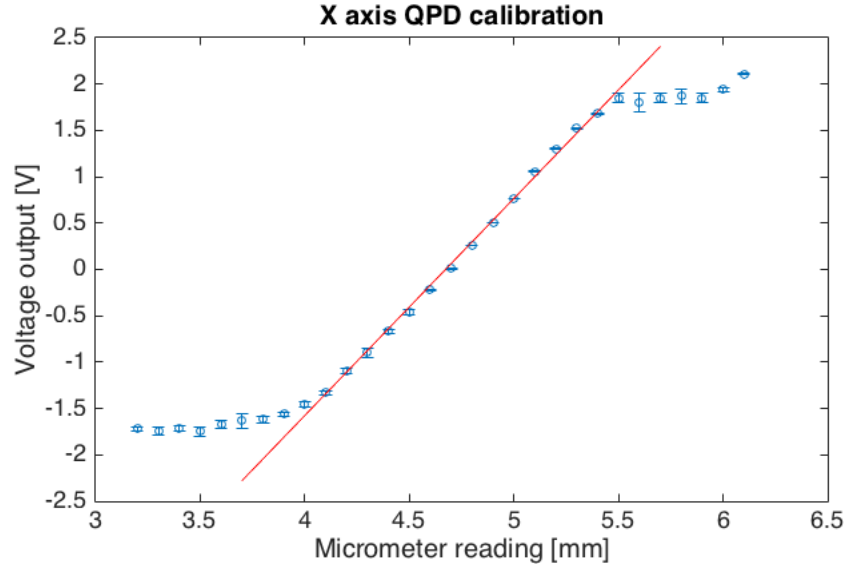 $$f(x) = ax + b \tag{2.1}$$

  returns: $a = (2.34 \pm 0.02)$ V/mm; $b = (-10.942 \pm 0.004)$ V, where a gives us the Volts/displacement ratio.

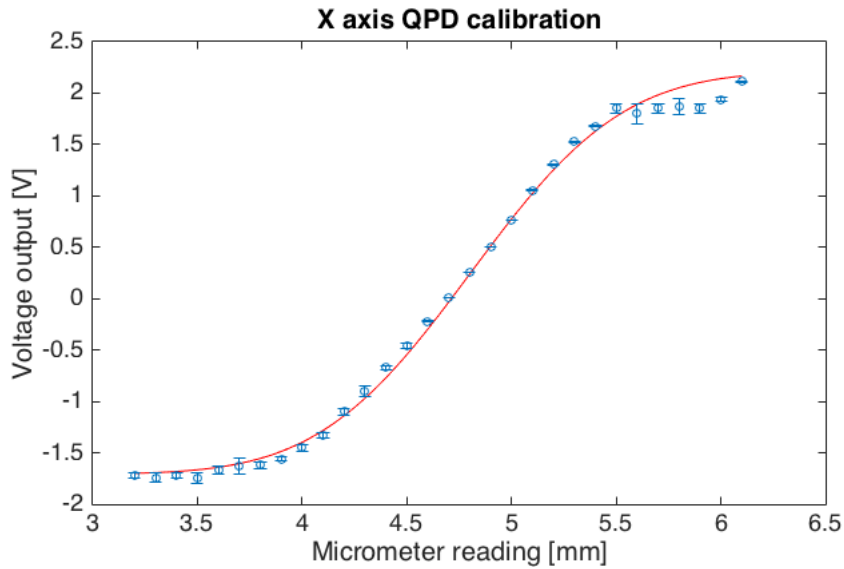 The plot in figure 2.2(b) shows the fit of the QPD calibration curve with the error function:

  $$f(x) = a_1 + b_1 \cdot erf(c_1 x + d_1) \tag{2.2}$$

  The QPD X output is a voltage given by:

  $$\Delta V = \alpha(P_{right} - P_{left}) \tag{2.3}$$

X axis QPD calibration

(a)

X axis QPD calibration

(b)

Figure 2.2: X axis QPD calibration curves.

where α is a constant and $P_{right} - P_{left}$ is the difference between the power on the right and left sides of the QPD. From the gaussianity of the beam it follows:

$$\Delta V = \alpha P_0 \cdot erf\left(\frac{\sqrt{2}(x - x_0)}{w_x}\right) \tag{2.4}$$

where P_0 is the total power transmitted by the beam, x is the distance from the beam's center to the QPD center, x_0 is an offset and w_x is the beam radius. Equation 2.4 can then be used together with fit results to obtain:
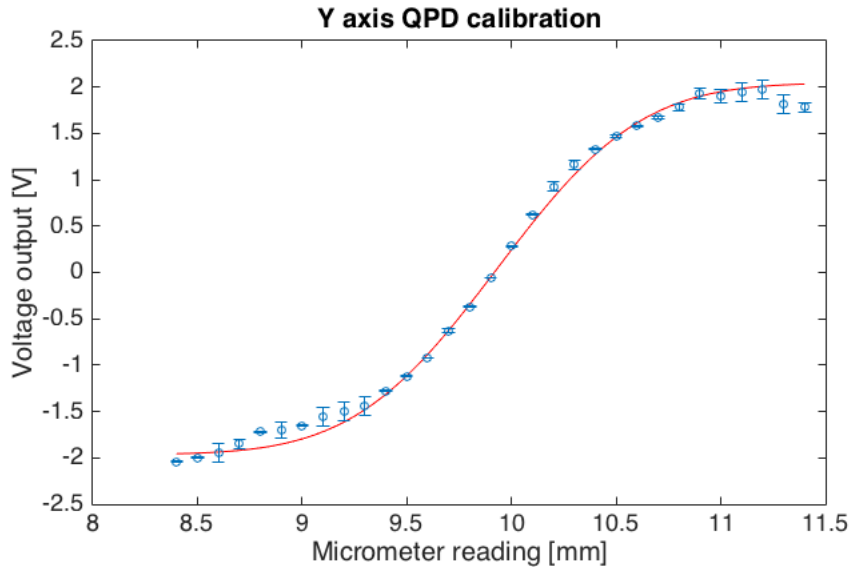
$$w_x = 1.14 \ mm$$

$x_0 = 4.81 \ mm$

- Y axis calibration

  Figures 2.3(a) and 2.3(b) show the fit in the linear region and the error function fit for the Y axis calibration, respectively.
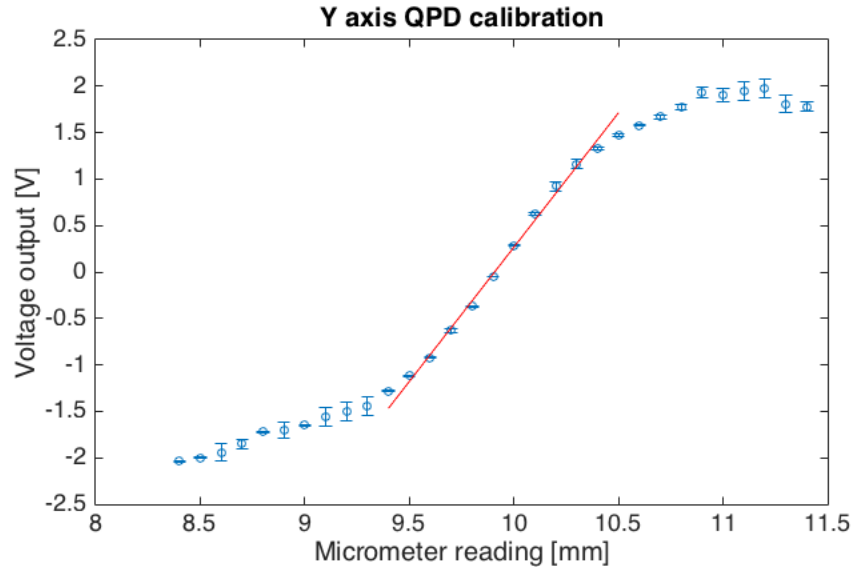
(a)

(b)

Figure 2.3: Y axis QPD calibration curves.

The first fit with the function:

$$f(x) = px + q \tag{2.5}$$

returns: $p = (2.89 \pm 0.03)$ V/mm; $q = (-28.647 \pm 0.003 \ )$V, where p gives us the

Volt/displacement ratio.

The non-linear fit is made with the function:

$$f(x) = a_2 + b_2 \cdot erf(c_2 x + d_2) \tag{2.6}$$

The expression for the QPD's Y output is analogous to the one for the X axis:

$$\Delta V = \alpha P_0 \cdot erf\left(\frac{\sqrt{2}(y - y_0)}{w_y}\right) \tag{2.7}$$

and form fit results, in this case, we obtain:

$w_x = 1.08$ mm;
$y_0 = 9.93$ mm

We notice that w_x and w_y are both compatible with the beam spot size we observed in laboratory.

2.1.2   Measured resonant frequencies

In order to measure the rhomboid resonant frequencies, the oscillation mode of interest was excited and the resonant frequency measured as explained above. The photosensors were used for the measurement of the tilt and pendulum resonant frequencies, while the QPD was used to measure the yaw resonant frequency. Results are shown in table 2.1.

Mode	Frequency 1 (mHz)	Frequency 2 (mHz)
tilt	108±1	2352±28
pendulum	645±5	615 ± 5
yaw	139.5±0.5	

Table 2.1: Rhomboid resonant frequencies. The second column (Frequency 1) shows the frequencies for oscillations along the long side of the rhomboid, while the third one (Frequency 2) shows the frequencies for oscillations along the short side.

The oscillation modes of interest are the tilt and pendulum resonant frequencies shown in the second column. Results show that a low tilt resonant frequency is reached, but in order to reach an even lower one (~ 40 mHz) we need to increase the distance between the rhomboid center of mass and the suspension point.

2.2   The inverted pendulum

In this section the procedure used to determine the IP parameters that could reduce its resonant frequency to as low as 40 mHz is shown.
To approach this problem we can start by considering a simple shape of the IP and then apply the results obtained to the final shape of IP.

2.2.1 A simple model of the inverted pendulum

A really simple IP is made of a flexure at the bottom, a cylindrical rod and a spherical mass on top as in figure 2.4.
The resonant frequency for this IP is given by:

$$f_0 = \frac{1}{2\pi}\sqrt{\frac{k}{I} - \frac{g}{I}[m_1\frac{l_1}{2} + m_2\left(l_1 + \frac{l_2}{2}\right) + m_3(l_1 + l_2 + r_3)]} \tag{2.8}$$

where k is the IP spring constant, while r_1, l_1, m_1 and r_2, l_2, m_2 are respectively the bottom and top cylinder radius, length and mass. I is the IP moment of inertia about the axis perpendicular to the pendulum and passing through the point of rotation.

$\mathbf{m_3, r_3}$

$\mathbf{m_2, r_2, l_2}$
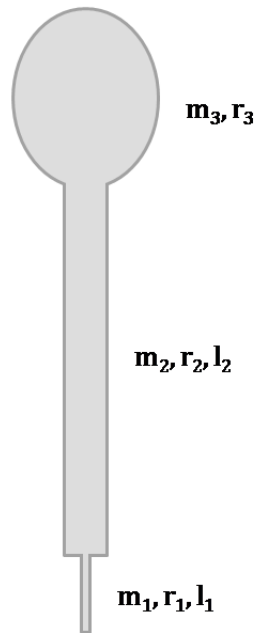
$\mathbf{m_1, r_1, l_1}$

Figure 2.4:

As from equation 2.8 the IP resonant frequency depends on its spring constant k. Thus, in order to reach a very low resonant frequency, k needs to be small. k depends on the bottom cylinder (flexure) parameters, therefore those parameters have to be determined.

In order to do this, an IP with the described shape was modeled using Comsol and its spring constant was calculated for different reasonable parameters of the bottom cylinder. The IP was built of stainless steel and with a total length of 41 cm, which is a good estimate for the real IP length.
The procedure used to calculate k consists in applying a force $F = 1\ N$ to the top of the sphere, perpendicular to the IP and then measure the IP displacement x on Comsol, as in figure 2.5. In the absence of gravity and in steady-state (as on Comsol) the equation of motion for the IP with the application of F is:

$$-k\theta + (l_1 + l_2 + 2r_3)F\cos\theta = 0 \tag{2.9}$$

where θ is the angular displacement of the IP. In the small angles approximation we obtain:

$$k = \frac{(l_1 + l_2 + 2r_3)^2 F}{x} \tag{2.10}$$
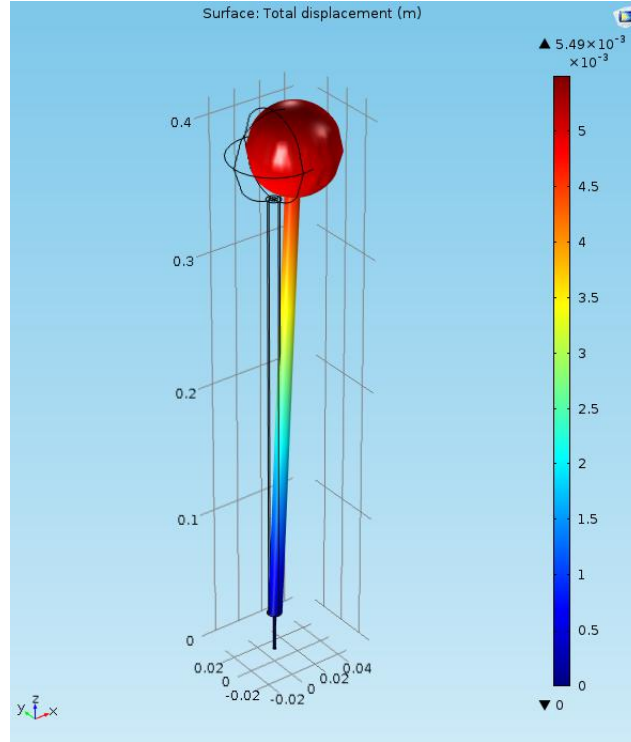
Thus x gives us k.

Figure 2.5: IP displacement on Comsol after the application of a force of 1 N to the top of the sphere.

After the determination of k for different reasonable parameters we can use equation 2.8 to determine the resonant frequency reached by the IP using each of them. Then we can choose the parameters which lead to the lowest f_0.

The best parameters selected for the IP with this method are: $r_1 = 0.7~mm$; $l_1 = 3~cm$. With those parameters the sphere mass needed to reach a resonant frequency of 40 mHz is expected to be $m_3 \simeq 1.2~kg$.

In any case, there is a limitation in trying to obtain a very small k, which is due to buckling. Comsol allows the study of linear buckling and returns the critical load factor (CLF), which is the ratio of the buckling loads to the applied loads. With the selected parameters Comsol returns CLF=1.03. This value is close to CLF=1 whereby significant buckling is expected, therefore we cannot push the cylinder dimensions too far: the selected parameters are already very near to the critical point.

2.2.2 Model for the final inverted pendulum

The final IP shape is shown in a Comsol model in figure 2.6(*a*). The IP has three legs of stainless steel, each with two identical flexures, and the top mass, of aluminum, has the shape of a parallelepiped. This parallelepiped is cut from the top part of the rhomboid, as in the final set up the relative distance between the rhomboid and the IP top mass is exactly what the Michelson interferometer measures. The number of legs is chosen in order to make the block stable, as it should not tilt, while their position is chosen in order to have a softer oscillation along the long side of the IP, which is the oscillation of interest. Moreover, each leg has a double flexure instead of just one in order to make the IP more sensitive to ground motion.

This structure is quite complex to analyze directly, thus we can start considering a more simple IP with the same block mass on top and just one leg as in figure 2.6(*b*).

The resonant frequency for this inverted pendulum is:

$$f_0 = \frac{1}{2\pi}\sqrt{\frac{k}{I} - \frac{g}{I}\left[m_1(2l_1 + l_2) + m_2\left(l_1 + \frac{l_2}{2}\right) + m_3\left(2l_1 + l_2 + \frac{c_3}{2}\right) + m_4\left(2l_1 + l_2 + c_3 + \frac{c_4}{2}\right)\right]}$$
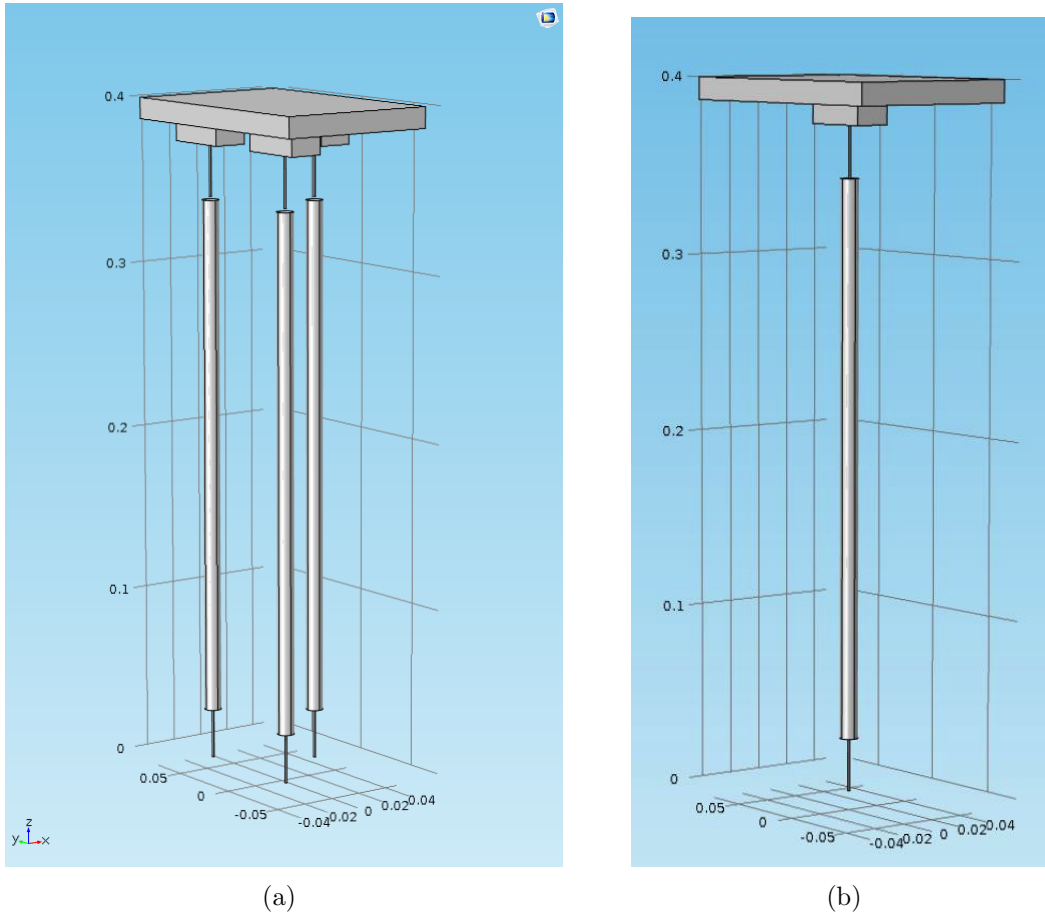
(2.11)

(a)   (b)

Figure 2.6: Inverted pendulum models on Comsol

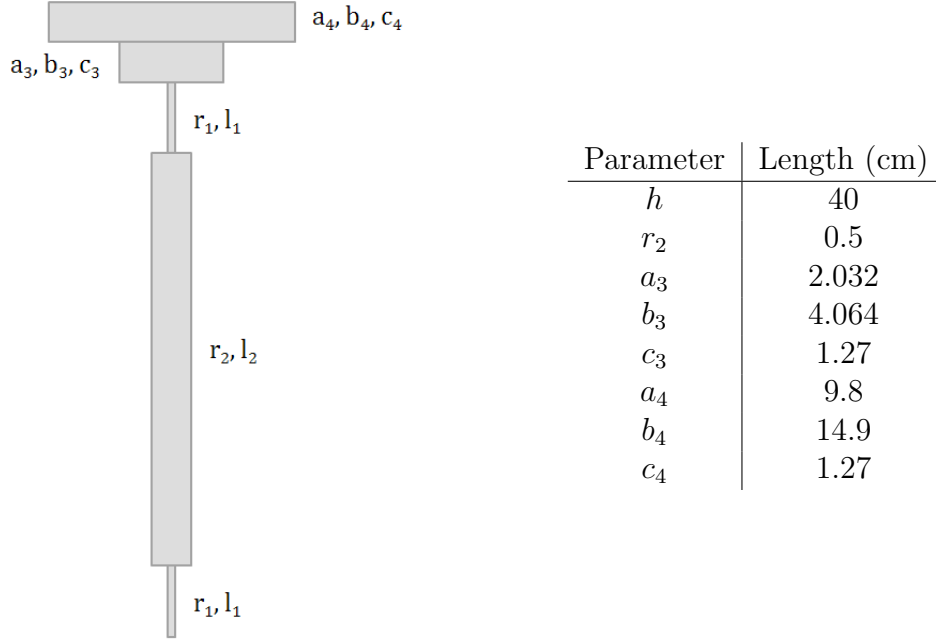| Parameter	Length (cm)
h	40
r_2	0.5
a_3	2.032
b_3	4.064
c_3	1.27
a_4	9.8
b_4	14.9
c_4	1.27

Figure 2.7: Inverted pendulum parameters

where we used the same notation for the cylinders as in the previous paragraph while a_3, b_3, c_3 and a_4, b_4, c_4 are respectively width, depth and height for the first and the second block (see fig. 2.7). We are also going to call h the total length of the leg (including the first block[1]).

The moment of inertia, I for the oscillation along the long side of the block is:

$$I = \frac{1}{2}m_1 r_1^2 + \frac{1}{6}m_1 l_1^2 + m_1 \left(\frac{l_1}{2}\right)^2 + \frac{1}{4}m_2 r_2^2 + \frac{1}{12}m_2 l_2^2 + m_2 \left(l_1 + \frac{l_2}{2}\right)^2 + m_1 \left(\frac{3}{2}l_1 + l_2\right)^2 + \\ + \frac{1}{12}m_3 \left(b_3^2 + c_3^2\right) + m_3 \left(2l_1 + l_2 + \frac{c_3}{2}\right)^2 + \frac{1}{12}m_4(b_4^2 + c_4^2) + m_4 \left(2l_1 + l_2 + c_3 + \frac{c_4}{2}\right)^2 \tag{2.12}$$

Some of these parameters are fixed by the dimensions of the rhomboid and they are shown in the table in figure 2.7.

We can do some considerations to use equation 2.11 for our three-legs inverted pendulum. We can think of the three legs of the inverted pendulum as three springs in parallel, each with a spring constant k'. Thus the three legs are equivalent to one leg with spring constant $k = 3k'$.

Another consideration we have to do in order to use equation 2.11 for our three-legs inverted pendulum is that if we pass from three to one leg, in order to conserve the mass and moment of inertia of the structure we have to use a thicker leg, for example of double radius. This method is, of course, an approximate method, but it can give us a coarse estimate of

---

[1]This block will be necessary to hold the legs in the real final IP

the resonant frequency of the final inverted pendulum. Using this estimate we can select the IP parameters needed to reach a reasonant frequency of ~ 40 mHz.

2.2.3   Parameters determination

Different parameters for the legs flexures were chosen based on the results from the simple IP model in previous paragraph. The flexure length was chosen as $l_1 = 3.2\ cm$ while the selected radii were: $r_1 = (1;\ 0.7;\ 0.5)\ mm$.
$k = 3k'$ was both determined with Comsol and experimentally doing the following:

Observation: consider a single leg with a double flexure. Let x be the displacement obtained applying an horizontal force on the top of the leg, assuming that the top part of the leg can only roll (as it happens in the final IP). This displacement is half of the displacement we will obtain considering a single flexure leg of half height, while applying the same force on top of it. This means that the spring constant k' of a double flexure leg is $k' = 2k''$ where k'' is the spring constant of the single flexure leg of half height. It follows that the spring constant of the three-legs inverted pendulum is $k = 6k''$.

- k'' from Comsol

  k'' can be obtained with Comsol building a single flexure stainless steel structure of half the total leg height (let it be l) and applying a horizontal force on top of it as in figure 2.8(a). k'' is given by:

  $$k'' = \frac{l^2 F}{x} \tag{2.13}$$

- k'' determined experimentally

  In order to measure k'' experimentally for each selected rod, an inverted pendulum made of a single flexure in stainless steel (of 3.2 cm length and selected radius), two pin-vises and a top mass was assembled. By placing the IP in horizontal position and measuring the mass displacement caused by gravity (see fig. 2.8(b)), k'' can be calculated.

Results for k'' calculated with Comsol and experimentally are shown in table 2.2.

Diameter (mm)	Measured k'' (Nm)	Comsol k''
0.98	0.295	0.405
1.40	1.188	1.559
1.99	1.507	6.002

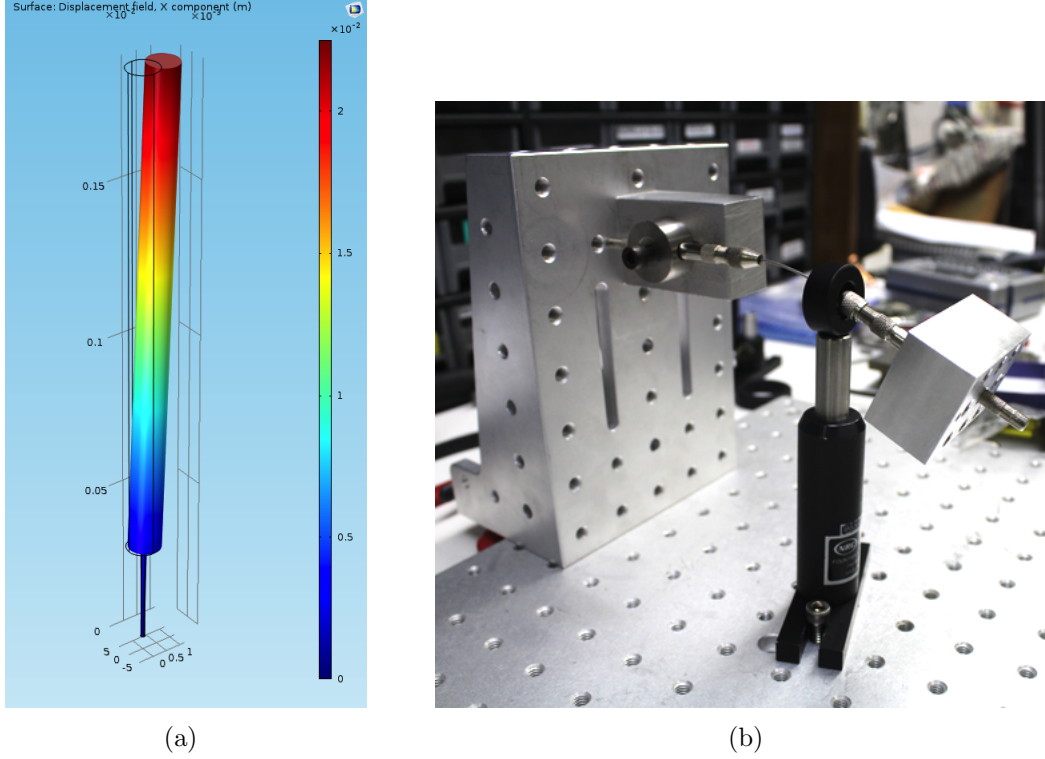Table 2.2: Values of k'' determined experimentally and using Comsol

(a)   (b)

Figure 2.8: Determination of k'' with Comsol and experimentally

The table shows a discrepancy between measured k'' and k'' from Comsol. Probably this discrepancy is due to the fact that in the real inverted pendulum the use of pin-vises generates clamping of the rod, while in the Comsol model this clamping is absent. Results also suggest that this clamping gets more significant as the rod radius increases. The discrepancy may also be related to the fact that the material we are using has not the same exact properties as the one used by Comsol. In any case, we decided to use the measured values for k'', as they are more reliable.

The inverted pendulums built with the three different rods are also used to get a coarse estimate of the quality factor for the final three-legs inverted pendulum.
The quality factor (Q) for our inverted pendulum is mostly related to structural damping, which, together with buckling, represents a limit in the achievement of a very low resonant frequency: if Q is too low there aren't oscillations, and the IP can't be used. It follows that a quality factor estimate is essential for the inverted pendulum parameters choice. The setup used to measure the quality factor for the three inverted pendulums is shown in figure 2.9. A LED light hits the IP top mass and the reflected light is detected by two photosensors.

When a small force is applied to the top mass the pendulum starts oscillating and the mass displacements can be read on an oscilloscope connected to the photosensors. The resonant frequency can be directly measured with the oscilloscope, while the quality factor can be calculated. As a matter of fact, our IP impulse response can be approximated by:

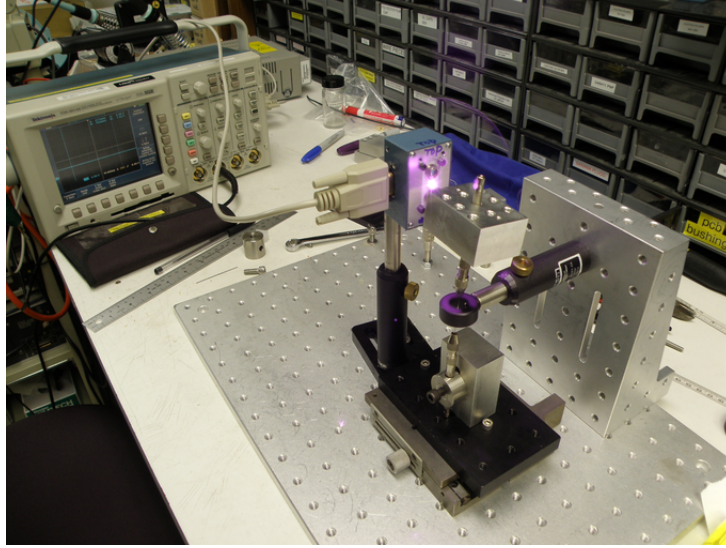$$h(t) = cos(2\pi f_0 t) \cdot exp(\frac{-\pi f_0 t}{Q}) \tag{2.14}$$

Figure 2.9: Quality factor measurement setup

where f_0 is the natural frequency of the IP.

The times at which the peak amplitude occurs are given by $t_j = \frac{j}{2f_0}$.

From these expressions we obtain:

$$\frac{h(t_j + 2)}{h(t_j)} = e^{\frac{-\pi}{Q}} \tag{2.15}$$

Thus, Q can be deduced from a measurement of the amplitude of the oscillation peaks.

The quality factor was calculated for the three inverted pendulums and, using that value, Q was deduced for the final IP with the following considerations.

The main dissipation mechanism in our inverted pendulums is structural damping. When this structural damping occurs the IP spring constant gets an imaginary term:

$$k \rightarrow k(1 + i\phi) \tag{2.16}$$

and the quality factor can be approximated as ([8]):

$$Q \approx \frac{1}{\phi} \frac{\omega_0^2}{\omega_0^2 + \frac{g}{l}} \tag{2.17}$$

where ω_0 is the angular natural frequency.

Thus, we can calculate ϕ from the measured Q and multiply this value by 6 in order to have ϕ' for our three legs IP. Then equation 2.17 can be used to estimate the quality factor at 40 mHz.

Results for ϕ were $\phi = 0.066$ using the 0.98 mm diameter rod; $\phi = 9.18 \cdot 10^{-3}$ for the 1.4 mm diameter rod and $\phi = 0.022$ for the 1.99 mm diameter rod.

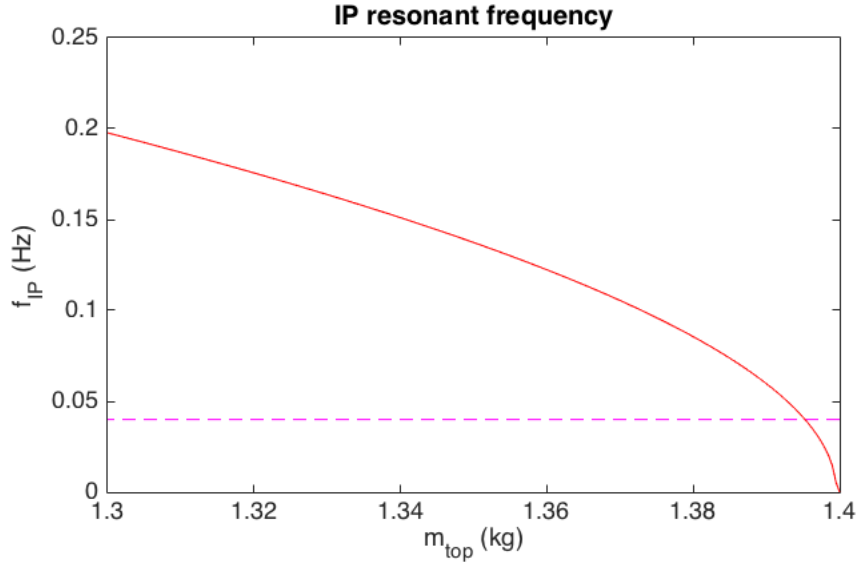These results determine the choice of the 1.4 mm diameter rod, as it is the one that leads to

Figure 2.10: Final IP resonant frequency dependence on the top mass

the highest quality factor. Also, the 0.98 mm diameter rod is too narrow, and it is subject to buckling for values of the mass on top of 1.2 Kg (value estimated from the simple inverted pendulum model).

At 40 mHz the quality factor for the selected rod results in $Q \approx 0.047$ which means that the IP is overdamped. However, in this simulation we assumed to have clamping of the rods, which leads to high structural damping, while in the final IP this clamping will be avoided as pin vises will not be used. We can then expect this Q to be higher in the final IP.

Using equation 2.11 we can also calculate the expected required mass on top of the IP to reach 40 mHz with the value of k'' from figure 2.7. As shown in figure 2.10 this mass results $m_4 \simeq 1.4 \ kg$.

We can then conclude that the selected parameters for our IP are the ones in table 2.3.

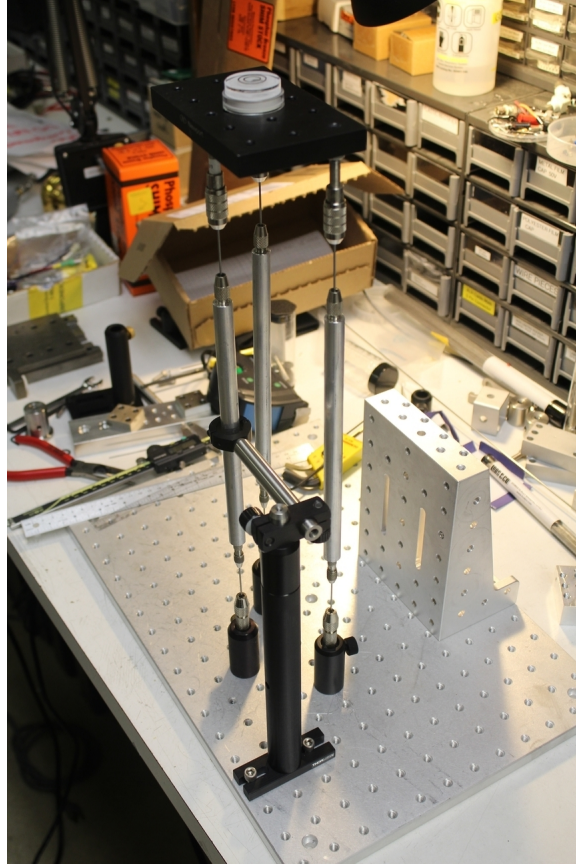| Parameter	Value (cm)
r_1	0.07
l_1	3.2
r_2	0.5
l_2	31.06

Table 2.3: Final inverted pendulum parameters

Figure 2.11: A prototype of the inverted pendulum

2.2.4 Prototype of the IP

In order to verify experimentally the possibility of having an inverted pendulum with a resonant frequency of 40 mHz with the selected leg parameters, such a pendulum was built and it is shown in figure 2.11.
The block of dimensions a_3, b_3, c_3 is not included in this prototype pendulum, and also the top mass is smaller than the one that will be used for the final inverted pendulum, but these differences are not too relevant in order to explore the possibility of reaching the desired 40 mHz.

The resonant frequency for the built inverted pendulum was measured using the procedure described in the previous paragraph for different masses added to the top. Measured resonant frequency values are plotted in figure 2.12. The data plot does not exactly match the resonant frequency predicted by equation 2.11. However, that equation is just an estimate of the resonant frequency and, also, to increase the mass on top of the IP we used aluminum blocks, thus the moment of inertia and length of the IP were not kept constant as in equation 2.11.

Low resonant frequencies ($\sim$ tens of mHz) were reached and, at those frequencies, a small mass variation lead to an unstable state. This shows that, for the built IP, a resonant frequency of $\sim$40 mHz can be achieved.
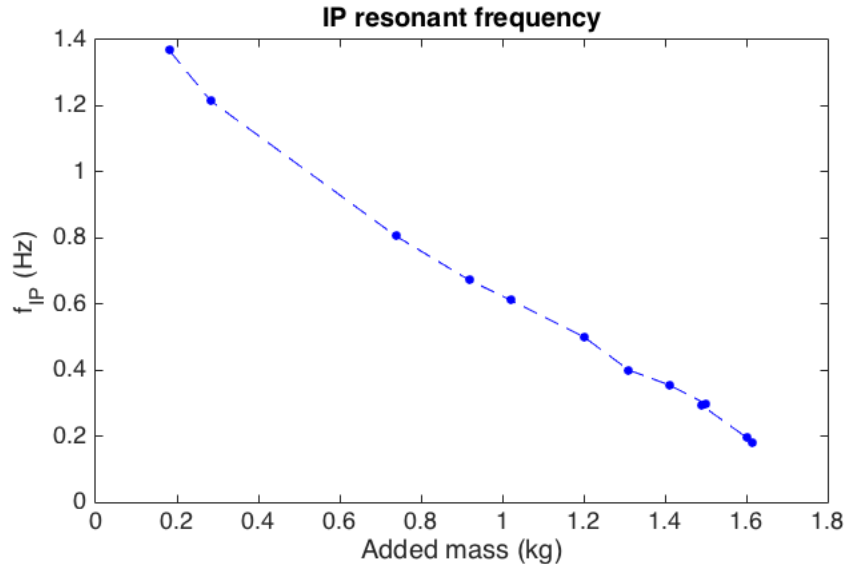
Figure 2.12: Prototype inverted pendulum measured resonant frequency vs. added mass

2.3   Temperature stabilization of the seismometer

In order to have very accurate measurements of ground displacements it is necessary to have the seismometer's temperature constant. As a matter of fact, if the temperature changes what basically happens is that the steel wires used to suspend the rhomboid change their lengths, and this affects the resonant frequencies of the rhomboid.
A thermal enclosure was then built (by Kelley et al. [9]) in order to keep the seismometer temperature constant. It is made of aluminum sheets covered by foam insulation and installed on the seismometer frame. Inside the enclosure are placed two heaters (on opposite faces) and four thermistors (in different positions). One of those thermistors is connected to a temperature controller which is used to drive the heaters, while the others are connected to another controller which is used only to compare temperatures in different areas of the enclosure.

2.3.1   Thermal enclosure tests

Two tests of the thermal enclosure were made to see how it behaves when temperature increases and decreases in an environment where room temperature is ~ 22 °C.

- Increasing temperature

  Using the controller (with P=250, I=0, D=0) the enclosure target temperature was set to 35 °C, and measurements of the temperature were taken starting from room temperature (20.1 °C) using the thermistor attached near to one of the heaters. Results are shown in figure 2.13, where a double exponential fit is made with the curve:
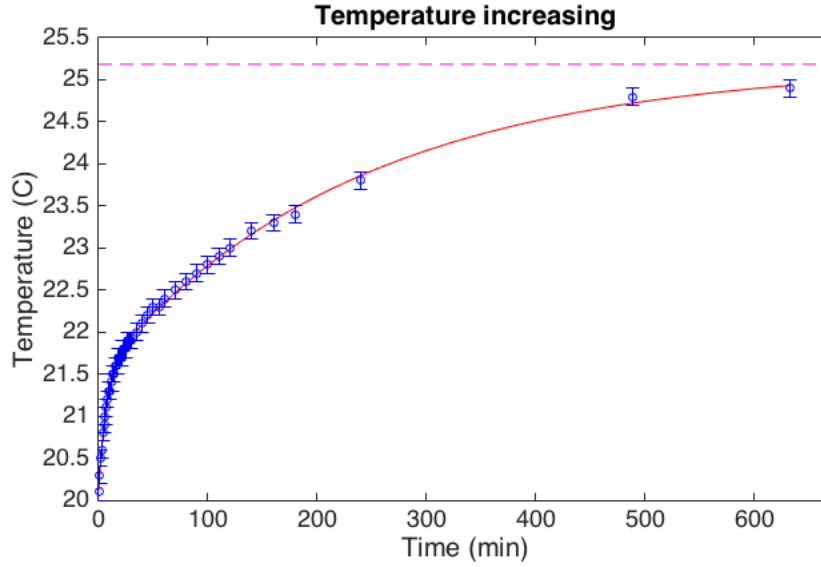
Figure 2.13: Thermal enclosure behavior: increasing temperature

$$f(t) = -a \cdot exp\left(\frac{-t}{\tau_1}\right) - b \cdot exp\left(\frac{-t}{\tau_2}\right) + c \tag{2.18}$$

and the fit results are:

$a = 3.739$ °C
$b = 1.1424$ °C
$c = 25.28$ °C
$\tau_1 = 247.1$ min
$\tau_2 = 7.49$ min

We see that the set temperature of $35\,°\mathrm{C}$ is not reached: the enclosure reaches just $25\,°\mathrm{C}$. Moreover, the $25\,°\mathrm{C}$ are reached with a double exponential behavior and not with the expected single exponential: this suggests that the thermal enclosure has some heat leak.

- Decreasing temperature

The decreasing temperature was measured by turning off the heaters and starting from a temperature of $24.3\,°\mathrm{C}$. Results are shown in figure 2.14, where the double exponential fit with the function:

$$f(t) = a' \cdot exp\left(\frac{-t}{\tau_1'}\right) + b' \cdot exp\left(\frac{-t}{\tau_2'}\right) + c' \tag{2.19}$$

returns:
$a'=2.03$ °C
$b'=1.22$ °C
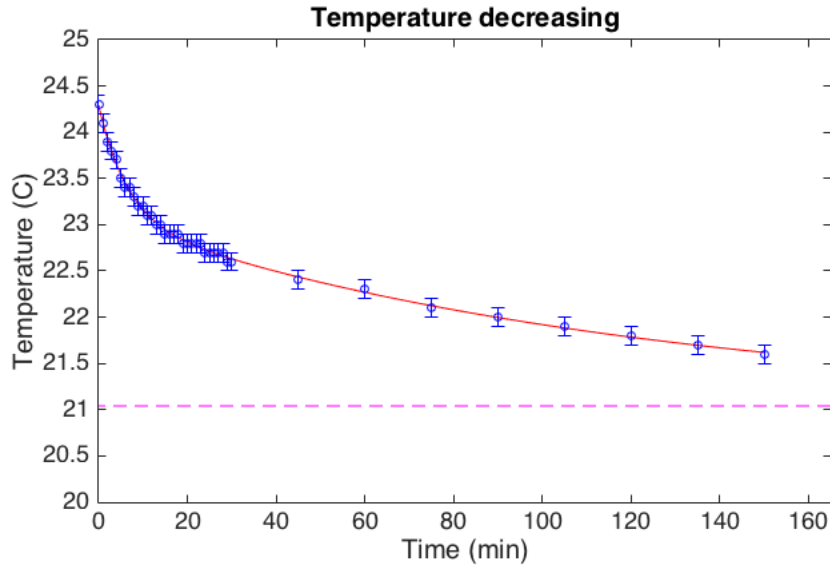
Figure 2.14: Thermal enclosure behavior:decreasing temperature

c'=21.04 °C
τ_1'=119.5 min
τ_2'=6.39 min

Again the double exponential trend of the box is shown.

As shown by Kelley ([9]), if the enclosure has a single heat capacity the temperature dependence on time is a single exponential. Thus, this double exponential trend of the enclosure seems to suggest that the enclosure has two heat capacities and a leakage.

2.3.2 Temperature stabilization

The thermal enclosure test shows that the equilibrium temperatures with the heater on and off are respectively 25 °C and 20 °C. We're interested in knowing how the temperature stabilizes. In order to do this we can set the target temperature between the two equilibrium temperatures and see how this temperature is reached. This has been done for both deceasing and increasing temperature.

- Decreasing temperature

  Using the controller (with P= 250, I=250, D=0) target temperature was set to 22 °C, while initial temperature was 23 °C. Results are shown in figure 2.15.

- Increasing temperature

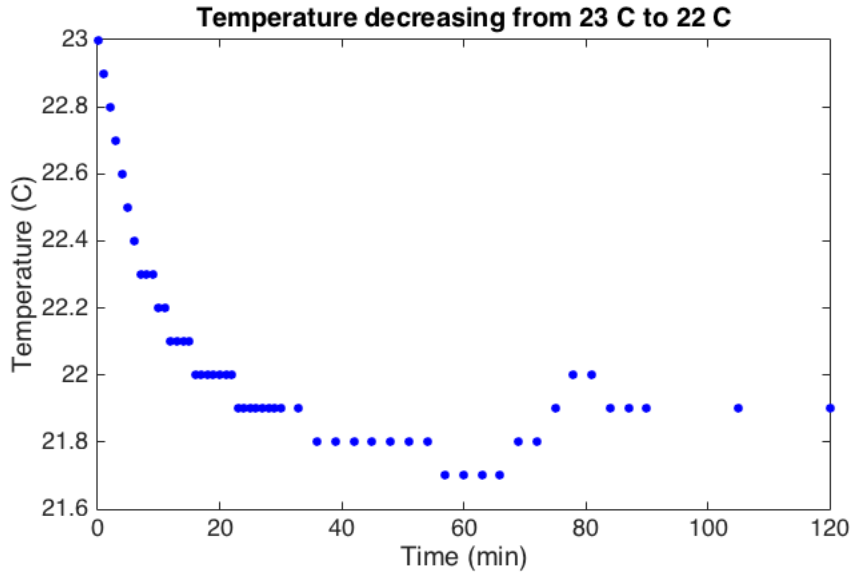 Initial temperature was 22 °C and target temperature was 23 °C. In this case we

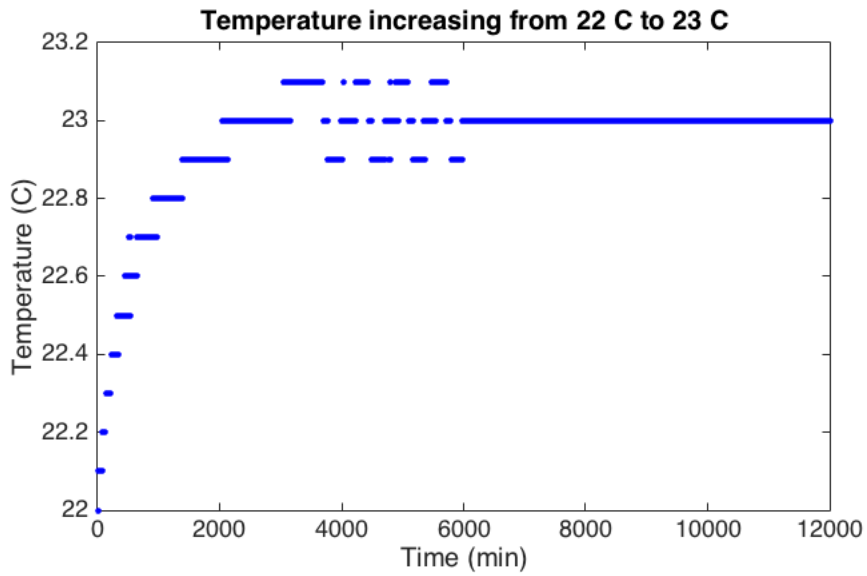Figure 2.15: Temperature stabilization: from 23 to 22 °C

Figure 2.16: Temperature stabilization: from 22 to 23 C

used a continuous data acquisition so that we could have more data with respect to the previous measurement, and results are shown in figure 2.16.

Results show that temperature stabilization is achieved for a temperature set between the two equilibrium temperatures.

3 Conclusions and future work

In this paper I described my work on a prototype for a tilt-free seismometer concerning its rhomboid, inverted pendulum and thermal enclosure parts.
From the results obtained for rhomboid resonant frequencies it follows that we need to tune the rhomboid suspensions and structure to reach a lower tilt resonant frequency, as we want to increase the seismometer sensitivity region.
Parameters to build the inverted pendulum for the seismometer were selected. Moreover, with a prototype of an inverted pendulum built with those parameters, we found that it is possible to achieve low resonant frequencies. However, for this built inverted pendulum the Q-factor was low, therefore it is necessary to build an IP where structural damping is reduced (i.e. without the use of pin-vises). Also buckling of the flexures needs to be studied carefully.
Results for the thermal enclosure show that the goal of having a structure which keeps the seismometer temperature constant is achieved. However the performance of the enclosure has to be improved since tests done on it show that heat leakage is present and due to imperfections in the structure. Moreover, in order to quantify the heat leakage, a model of the thermal enclosure should be developed.

Acknowledgements

References

[1] G. Cella and A. Giazotto *Interferometric gravity wave detectors.* Review of Scientific Instruments 82, 101 101 (2011).

[2] R. Adhikari, *Gravitational Radiation Detection with Laser Interferometry.* Reviews of Modern Physics 86, 121 (2014).

[3] K. Dooley, *Seismic Isolation.* Presentation for LIGO SURF, LIGO-G1500851-v1 (2015).

[4] F. Matichard, M. Evans *Review: Tilt-Free Low-Noise Seismometry.* Bulletin of the Seismological Society of America, Vol. 105, No. 2A (2015).

[5] K. Dooley, S. Moon, K. Arai, R. Adhikari *Towards a tilt-free seismometer design.* Poster at March LVC Meeting, DCC-G1500315-v1 (2015).

[6] F. Matichard, B. Shapiro, N. Robertson, H. Radkins, B. Lantz, R.Mittleman, *An overview of Advanced LIGO combination of passive and active vibration isolation.* LIGO-P1500165-v3 (2015).

[7] F. Matichard, R. Mittleman, M. Evans, *On the mechanical filtering of the transmission of tilt motion from ground to horizontal inertial sensors.* Pre-print for submission to the Bulletin of the Seismological Society of America (2015).

[8] G.Losurdo, *Ultra-Low Frequency Inverted Pendulum for the VIRGO Test Mass Suspension.* Thesis, LIGO-P980008-x0 (1998).

[9] M. Kelley, *Prototyping a tilt-free seismometer, Final Report.* LIGO-T1500218-v1 (2015).